communications earth & environment

Article

A Nature Portfolio journal

https://doi.org/10.1038/s43247-026-03397-z

Monsoon-driven waves induce a prevailing recession in mangrove forests across the Ganges-Brahmaputra-Meghna Delta

Yuan Xiong[1], Zhijun Dai[1,2] ✉, Chuqi Long[3], Xuefei Mei[1,4], Jinping Cheng[3], Cong Mai Van[5], Binh An Nguyen[6] & David M. Kennedy[7]

The role of monsoon-induced wave action in driving mangrove loss in deltaic settings remains underexplored in comparison with the role of anthropogenic activities. Here, we reveal that the Ganges-Brahmaputra-Meghna Delta (GBMD), the world's largest mangrove ecosystem within a monsoon-dominated region, exhibited an increased trend in total mangrove area at a rate of 133.3 ± 6.7 ha yr^{-1} from 1988 to 2022, despite a landward retreat of the mangrove shoreline at 5.98 ± 1.56 m yr^{-1}. Monsoon-driven wave action is the primary driver of mangrove loss, with sea-level rise and tropical cyclones acting as critical amplifiers that exacerbate wave-driven erosion. In contrast, tidal currents promote sediment redistribution into channels, backshore areas, and around barrier islands and sandbanks, thereby fostering mangrove colonization and largely compensating for mangrove loss. Our findings highlight how southwest monsoon-induced waves drive mangrove loss, shedding light on the mechanisms underlying mangrove degradation in wave-dominated coastal areas.

Mangroves are salt-tolerant evergreen woody plants that grow on tropical and subtropical coasts[1,2]. Compared to other coastal ecosystems, mangroves are recognized for their significant role as reservoirs for "blue carbon" storage[3]. They also provide rich ecological value and are substantial attenuators of wave energy[4,5]. However, mangrove-rich coasts, especially those in monsoon-controlled zones such as Southeast Asia, have suffered the largest net loss of mangroves[6,7]. While there is an overall regional pattern of mangrove loss, at the local scale (e.g., Nanliu River delta, Beilun River delta, Red River delta, and Mekong River delta), there are increases in mangrove area[8]. Therefore, to better plan ecosystem restoration, a greater understanding is needed of mangrove forest dynamics at the site-specific scale.

Mangroves grow in the intertidal zone in areas and flourish in areas with a positive sediment supply[9]. Any change in local hydrodynamics and sediment flux will impact mangrove establishment, through changing the landscape's dynamics of the tidal flats on which they develop[10]. The relative stability of mangroves can be maintained if sediment supply can keep pace with sea-level rise, but where it is low, there is a risk of submergence of the community[1,5]. During periods of low wave energy, suspended sediment is deposited in the intertidal zone, allowing mangrove seedlings to establish[11]. However, periods of high wave energy cause sediment to be moved out of the system and create potential erosion hotspots, which makes mangroves vulnerable[12,13]. Tropical cyclones and typhoons will also topple trees or remove sediment from between mangrove roots[14], dramatically raising the risk of mangrove loss[15].

Human interventions also directly impact mangrove cover. Hydraulic engineering (e.g., upstream dams and barrages) and coastal construction (e.g., seawalls and groynes) alter water flow and sediment deposition, often reducing the rate of sediment supply needed to counteract erosion[16]. In addition, aquaculture, agriculture, and urban development also involve mangrove deforestation, thereby exacerbating erosion[17–19]. In spite of these threats, efforts to conserve and restore mangroves in many regions have led

[1]State Key Laboratory of Estuarine and Coastal Research, East China Normal University, Shanghai, China. [2]Laboratory for Marine Geology, Qingdao Marine Science and Technology Center, Qingdao, China. [3]Department of Science and Environmental Studies, The Education University of Hong Kong, Hong Kong, China. [4]Ocean Decade International Cooperation Center, Qingdao, China. [5]Faculty of Civil Engineering, Thuyloi University, Hanoi, Vietnam. [6]Department of Geography and Remote Sensing, Institute of Life Sciences, Vietnam Academy of Science and Technology, Ho Chi Minh City, Vietnam. [7]School of Geography, Earth and Atmospheric Science, The University of Melbourne, Parkville, Victoria, Australia. ✉e-mail: zjdai@sklec.ecnu.edu.cn

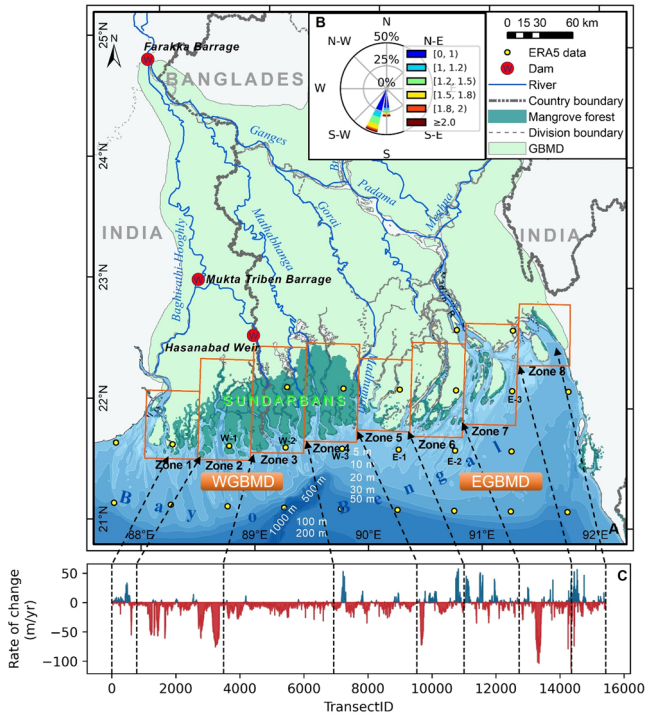

Fig. 1 | Study area and mangrove shoreline changes. The map in **A** displays the mangrove forest distribution (green shading, derived from this study) and the division boundaries. Red circles with 'W' mark the locations of dams and barrages, while yellow circles indicate the ERA5 reanalysis data points. **B** The inset shows the wave rose diagram representing wave conditions in 2022 (generated using ERA5 reanalysis data from ECMWF). **C** The profile shows the rate of mangrove shoreline change along the delta front from 1988 to 2022, calculated using the Digital Shoreline Analysis System (DSAS). Blue vertical lines indicate accretion, and red vertical lines indicate erosion. Note: WGBMD, Western GBMD; EGBMD, Eastern GBMD.

to localized expansion of these systems[20,21]. Fluvial deltaic regions often exhibit both accretion and erosion because their high sediment supply can counteract the stresses experiences[22], such as the Indus Estuary, Irrawaddy River Delta, and Mekong Delta[20,23,24], as well as Bangladesh[25–27].

The Ganges–Brahmaputra–Meghna Delta (GBMD) (Fig. 1A) hosts the largest mangrove area (approximately 1 million ha)[28,29] with most forests being legally protected within the Sundarbans Reserved Forest (Fig. 1A). The southwest monsoon, from June to September, is the primary seasonal driver of wind and wave dynamics. During this period, southwesterly winds drive the Southwest Monsoon Current (SMC) into the northern Bay of Bengal, generating enhanced wind-driven wave activity and surface currents[30]. Additionally, wave activity is occasionally amplified by cyclones[31]. This makes the southwest monsoon the main driver of nearshore wave formation in the region, along with contributions from remote swell and tidal currents[32] (Fig. 1B). How these dynamic changes arise, and which driving factors are responsible, remain largely unclear, greatly hindering our understanding of the mangroves' resilience and adaptive capacity across the large delta. Obtaining the latest information on the mangrove ecosystem in this area is extremely crucial for sustainable resource management, but the dense canopy in the intertidal zone presents challenges for conventional in situ monitoring. Therefore, we utilize multi-temporal Landsat remote sensing images and the Continuous Change Detection and Classification (CCDC) algorithm to analyze changes in mangrove coverage in the GBMD from 1988 to 2022. The objectives of this study are to: (1) map dynamic changes in mangrove extent; (2) identify the possible drivers of mangrove loss and gain; and (3) explore the effect of monsoon-driven waves on shifts in the mangrove shoreline. This study will describe the multi-year changing process of mangrove cover and mangrove shoreline position in GBMD, providing a data foundation and scientific basis for global and regional efforts to conserve mangrove ecosystems and support their sustainable management.

Results

Mangrove shoreline changes

In the GBMD, from 1988 to 2022, the mangrove shoreline exhibited a dominant erosional trend, although erosion and accretion processes coexisted spatially (Fig. 1C). Erosion transects accounted for 74.79% of the total transects, significantly surpassing accretion (22.76%) and stable (2.45%) transects (Table S1). The erosion intensity also exceeded accretion, with region-wide average rates of −10.04 m yr^{-1} and 6.61 m yr^{-1}, respectively. A visual comparison of mangrove patch boundaries between 1988 and 2022 confirms this widespread retreat (Figure S1).

The mangrove shoreline in the WGBMD also experienced pervasive erosion, with an average retreat rate of 7.33 m yr^{-1} (Table S1). Erosion transects accounted for 84.78% of the total transects, compared to only 13.18% for accretion (Table S1). The intensity of erosion also outweighed accretion processes. The maximum erosion rate reached −75.78 m yr^{-1} (Transect 3119, Zone 2) (Figure S2A), while the maximum accretion rate was 52.78 m yr^{-1} (Transect 7225, Zone 4) (Figure S2B). Zone 2 was identified as the most intensely eroded region, representing the southernmost active front of the GBMD. Severe erosion, with rates exceeding 50 m yr^{-1}, was concentrated in three specific segments: Transects 1218–1246, 2563–2582, and 3068–3229 (Fig. 1C, Figure S2A). Conversely, accretion was observed in localized pockets within the western parts of Zone 1 and Zone 4. Notable accretion hotspots (>10 m yr^{-1}) were specifically identified between Transects 421–488 (Zone 1) and 7188–7267 (Zone 4) (Fig. 1C, Figure S2B).

The EGBMD contained an alternating pattern of erosion and accretion, with an average shoreline change rate of −4.02 m yr^{-1} (Table S1). Transects exhibiting erosion accounted for 64.47% of the total transects, while accretion transects accounted for 31.92% (Table S1). Notably, this region recorded the most extreme change, with the maximum erosion rate reaching −112.88 m yr^{-1} at Transect 14330 (Zone 7) and the maximum accretion rate at 57.22 m yr^{-1} at Transect 10829 (Zone 5) (Fig. S2C, F). Spatially, Zone 5 and Zone 7 were identified as the most intensely eroded sectors. Severe retreat, with rates exceeding 50 m yr^{-1}, was concentrated in specific segments between Transects 9659–9722 and 13273–13410 (Fig. 1C, Fig. S2D, F). Conversely, shoreline accretion mainly occurred along the southwestern coast of Zone 5 and within Zone 6. Significant progradation, characterized by accretion rates exceeding 10 m yr^{-1}, was primarily observed across three distinct clusters: Transects 10774–10829, 11056–11157, and 11498–11597 (Fig. 1C, Fig. S2C, E).

Mangrove forest area changes

Between 1988 to 2022, the total mangrove forest area in the GBMD, increased from 648,822.1 to 653,670.7 ha (Fig. 2A). This increase followed four stages: (1) rapid growth (1988–2000): the mangrove area showed a fluctuating, rapid growth trend, increasing from 648,822.1 to 657,591.3 ha, with a growth rate of 988.3 ha yr^{-1}; (2) slow decline (2000–2009): the mangrove forests entered a slow decline phase, with the area decreasing to 654,329.5 ha, at a rate of −392.6 ha yr^{-1}; (3) recovery (2009–2016): the mangrove area began a slow fluctuating growth, reaching 656,798.1 ha, approximately the same as in 2000, with a growth rate of 354.9 ha yr^{-1}; and (4) accelerated decline (2016–2022): the trend reversed, with the mangrove area decreasing at a rate of −594.8 ha yr^{-1}, faster than the previous decline phase.

At a regional scale, the EGBMD generally mirrored the overall increasing trend (Fig. 2C); however, the WGBMD, which hosts the majority of the forest, showed a distinct and continuous long-term decline (Fig. 2B). Specifically, from 1988 to 2000, mangrove areas declined in both the western and eastern regions, at rates of 104.6 ha yr^{-1} and 1,092.9 ha yr^{-1}, respectively. From 2000 to 2009, both regions continued to lose mangrove cover, with the western region decreasing at 143.0 ha yr^{-1} and the eastern at a faster rate of 249.6 ha yr^{-1}, despite noticeable fluctuations in the west. From 2009 to 2016, the western and eastern regions' change rates were −55.4 ha yr^{-1}

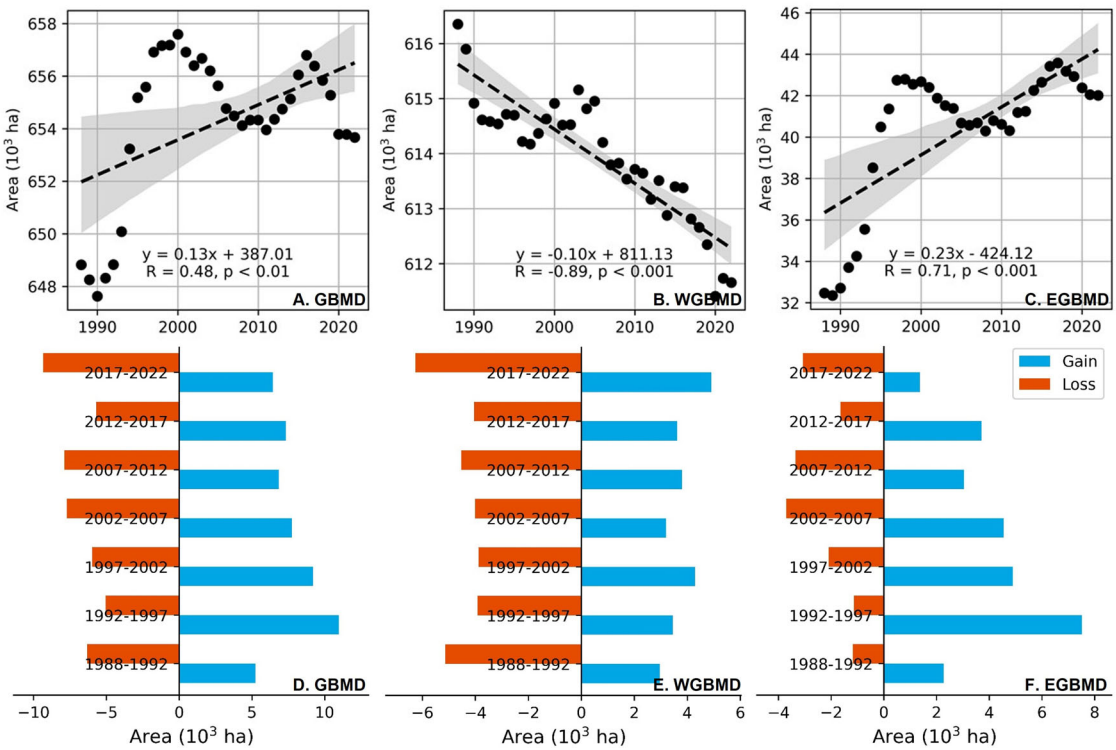

Fig. 2 | Spatiotemporal dynamics of mangrove forest area (1988–2022). **A**–**C** Show the temporal trends of the total mangrove forest area in the entire GBMD, WGBMD, and EGBMD. Black dots represent annual area data, and black dashed lines indicate the linear trend. The gray shaded areas denote the 95% confidence intervals. **D**–**F** Display the gains and losses of mangrove forest area across seven periods. Blue bars represent mangrove area gain, and orange bars represent mangrove area loss.

and 410.2 ha yr^{-1}, respectively. However, from 2016 to 2022, both regions showed a declining trend, with the western region losing mangroves at a faster rate (−306.1 ha yr^{-1}) than the eastern (−288.7 ha yr^{-1}).

Spatiotemporal patterns of gain and loss

The spatial variation of GBMD mangrove forests exhibits asynchrony. Between 1988 and 1992, the changes were relatively balanced, with a loss of 6311.1 ha and a gain of 5237.3 ha (Fig. 2D), especially in the WGBMD (Fig. 2E). Mangrove losses were observed along the shores of the GBMD (Fig. S3C, D, F), while notable gains occurred on the islands within the EGBMD (Fig. 2F, Fig. S3G). During the two subsequent periods (1992–1997 and 1997–2002), mangrove conditions improved markedly, with net gains reaching 2.18 and 1.54 times the net losses, respectively. In both phases, large areas of new mangroves continued to develop in the tidal channels of the WGBMD (Fig. S4A, B, E, Fig. S5A, B, E), and on the islands/sandbanks of the EGBMD (e.g., the landward sides of some barrier islands) (Fig. S4E, G, Fig. S5E, G). However, while gain within river channels increased, coastal mangrove decline became more pronounced, especially along the southwestern margins of the islands (Fig. S4A, B, F, Fig. S5A, B, F).

From 2002 to 2007, in addition to continued mangrove cover degradation (Fig. S6B, C, F), northern sections of larger islands in the EGBMD also experienced mangrove loss (Fig. S6G), totaling 7715.9 ha. Meanwhile, mangroves expanded further seaward, particularly toward the southern reaches of the delta, where smaller and more remote islands and sandbanks became focal points for establishment (Fig. S6D, E, G). The area increased to 7743.9 ha, effectively compensating for the losses during this period. From 2007 to 2012, the GBMD witnessed a total mangrove loss of 7882.0 ha, including severe degradation on islands near river mouths (Fig. S7G). However, in certain areas, such as tidal channels and the northern sides of islands, an increase in mangrove cover occurred (Fig. S7A, B, D, E), amounting to 6850.5 ha. From 2012 to 2017, mangrove losses in the GBMD amounted to 5689.0 ha, while gains reached 7330.6 ha. In the EGBMD, the trend of mangrove degradation slowed, with new mangroves forming on the southern parts of river sandbanks (Fig. S8D, E, G). Conversely, in the WGBMD, the mangrove shoreline retreated inland due to coastal erosion, with most losses occurring along the seaward mangrove shoreline (Fig. S8B–F). Meanwhile, isolated mangrove patches were established sporadically on newly accreted shoals within tidal channels (Fig. S8A, B). In the final period, from 2017 to 2022, significant mangrove losses were observed in the GBMD, with a total of 9344.6 ha lost and only 6439.4 ha gained. In addition to previously affected areas, large-scale mangrove depletion was observed near river mouths in the EGBMD (Fig. S9G). Although small-scale expansion was still detected along tidal channels in some parts of the GBMD (Fig. S9A–E), these gains were spatially confined to scattered segments of tidal channels and failed to form extensive, continuous patches.

Overall, from 1988 to 2022, the GBMD mangrove area experienced a gain of 42,581.2 ha. Significant expansion of mangroves was observed along the tidal channels in WGBMD, the estuarine sandbanks in EGBMD, and the southern parts of islands away from major estuaries. During the same period, the GBMD mangroves also suffered a loss of 37,452.9 ha, primarily at some seaward edges of the delta, with permanent mangrove destruction particularly severe along the WGBMD coast (Figs. S3–S9). Within the coastal zone specifically, mangroves exhibited a loss of 11,019.1 ha, and only 2085.0 ha gained seaward. This contrast highlights that, although the overall mangrove extent increased at the delta scale, coastal areas, particularly exposed shorelines, experienced substantial degradation.

Correlation between wave and shoreline changes

Analysis of long-term ERA5 wave data (1988–2022) reveals a distinct seasonal energy regime. The mean significant wave height during the monsoon season consistently exceeds the non-monsoon period, with 95th percentile extremes frequently surpassing 1.75 m (Fig. S10A). Spatially, the western sector experiences higher waves compared to the east, where wave heights peak in July-August (Fig. S10B). Superimposed on this seasonal rhythm are high-magnitude events; notably, Cyclone Sidr (2007), where hourly wave

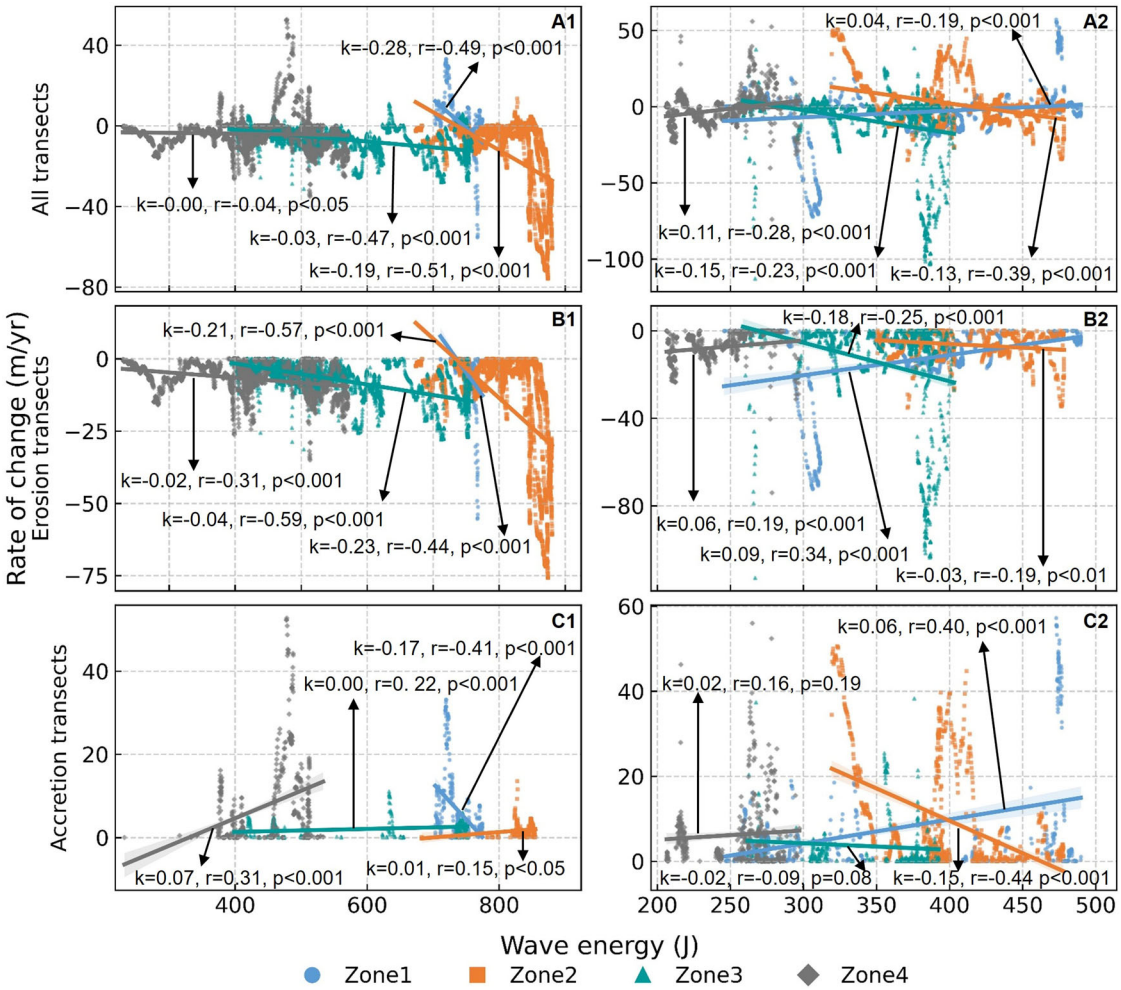

Fig. 3 | Linear regression analysis between wave energy (during monsoon) and shoreline change rates. The analysis includes all transects (**A**), erosion-only transects (**B**), and accretion-only transects (**C**). The left panels (**1**) represent the WGBMD (Zones 1–4), and the right panels (**2**) represent the EGBMD (Zones 5–8). Data series are distinguishing by color and shape: Zone 1/5 (blue circles), Zone 2/6 (orange squares), Zone 3/7 (teal triangles), and Zone 4/8 (gray diamonds). Solid lines represent the linear regression fits for each zone.

data recorded a significant wave height peaking at 5.1 m at station W-2 and 4.7 m at E-2 (Fig. S10C).

In the WGBMD (Zone 1–4), shoreline change rates exhibited a statistically significant inverse correlation with wave energy ($p < 0.001$), where higher energy consistently corresponded to accelerated erosion. This trend was particularly pronounced in erosion-only transects (Figure 3B1-2), with the correlation coefficient ranging from −0.30 to −0.59 (Table S2). In contrast, the EGBMD (Zones 5–8) displayed a spatially heterogeneous response (Fig. 3A–C2). While Zones 6 and 7 followed the erosional trend, Zones 5 and 8 exhibited anomalous positive correlations ($R = 0.19$ and 0.29, respectively). Consequently, no uniform region-wide inverse relationship between wave energy and shoreline change was observed in the EGBMD.

This wave-shoreline relationship is seasonal. In Zone 1, the regression slope steepened from −0.100 (non-monsoon) to −0.284 (monsoon). This indicates that waves cause nearly three times more erosion during the monsoon season. A similar increase occurred in other zones (Table S2).

Correlation between suspended sediment supply and mangrove area

River sediment supply also changed during the 35-year study period. The Ganges and Brahmaputra rivers showed a significant decreasing trend in suspended sediment discharge (SSD) (Fig. S11A). While the Meghna River remained relatively stable, the overall input to the delta system declined.

The relationship between the Suspended Sediment Concentration (SSC) and the change in mangrove forest area exhibits significant spatio-temporal lag, as detailed in Table S3. For the GBMD, the highest positive correlation ($r = 0.65$, $p < 0.001$) occurred with a 6-year lag. Regionally, the EGBMD also showed strong positive correlations at 6-year ($r = 0.65$, $p < 0.001$) lags. The response magnitude, quantified by the slope k, also peaked at this interval, with a value of 21.00. Contrarily, the WGBMD showed predominantly weak or negative correlations across the analyzed time lags (e.g., $r = -0.32$ at 7 years). The corresponding k values were consistently negative or near zero (e.g., $k = -4.31$ at 7 years).

Discussion

Ocean-atmosphere dynamics

Wave processes are major drivers of shoreline retreat in mangrove-dominated large deltas globally, such as the Irrawaddy and Indus[20,23]. In the GBMD, wave breaking can be observed on satellite imagery (Fig. 4A) with vertical erosion scarps (20–50 cm high) occurring in areas of long-term permanent mangrove retreat (Fig. 4B). Observations of exposed mangrove roots, not just pneumatophores, and remnants of dead trees on tidal flats (Fig. 4C, D), further suggest that waves contribute mangrove retreat in exposed areas. The WGBMD exhibits consistently negative regression slopes. Crucially, these slopes steepen threefold during the monsoon season (Table S2), indicating that the shoreline is sensitive to high-energy waves during this period. This amplification suggests that the shoreline is not

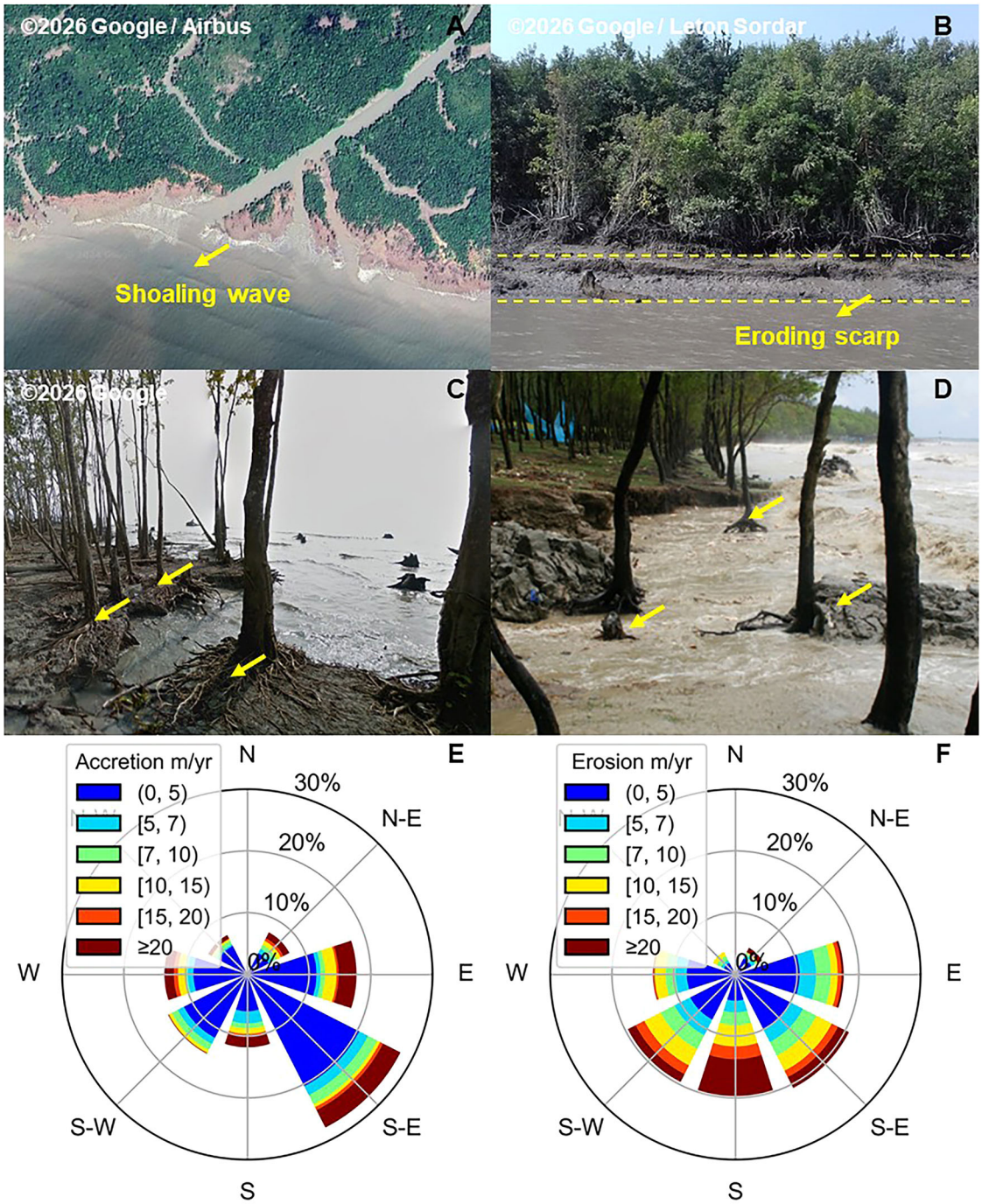

Fig. 4 | Field evidence of wave-induced erosion and shoreline orientation analysis. A Satellite view of shoaling wave about to break along the mangrove shoreline in the WGBMD (21°34′1.3″N, 88°50′48.7″E; Source: Google Map (https://maps.app.goo.gl/eWoCQhzS9jYo9iNaA)). **B** Erosion scarp at the seaward mangrove edge (May 2022, Sundarban National Forest; Photo credit: Leton Sordar; Source: Google Map (https://maps.app.goo.gl/rmjXfGWc7yoad2tE7)). The yellow dashed lines outline the scarp structure. **C** Mangrove trees with exposed roots on the coast. Yellow arrows indicate examples of exposed roots (Jan 2016, 21°50′38.3″N, 89°47′50.8″ E; Source: Google Map (https://maps.app.goo.gl/GtMCYmQ1md7JQcEJ8)). **D** Mangrove trees with residual stumps by waves crashing. Yellow arrows indicate examples of residual stumps[26]. **E**, **F** Show the rose diagrams for accretion and erosion shoreline azimuths, respectively.

merely responding to higher wave magnitude, but becomes structurally more vulnerable to erosion. Conversely, the EGBMD displays a heterogeneous response (Fig. 3). While wave energy remains high, the regression slopes are inconsistent, ranging from negative to anomalous positive values (Table S2). This heterogeneity demonstrates that the erosive capacity of waves is effectively masked or overridden by the immense sediment supply in the East. Consequently, the relationship between wave energy and shoreline change is decoupled in these accretion-dominated zones, distinguishing them from the wave-dominated Western delta.During the study period, 46 cyclones made landfall in the delta, mostly following a southwest-to-northeast trajectory (Fig. S12). Events like Cyclone Sidr (2007) generated mean significant waves up to 5.1 m high (Fig. S15C). Such extreme energy pulses cause immediate shoreline loss (Fig. S10C). On May 21, 2016, Tropical Storm Roanu made landfall[33,34], the mangrove forest experienced a decrease of 0.46% from 2016 to 2017 (Fig. 2C). From November 9−10, 2019, Tropical Cyclone Bulbul maintained high wind

speeds while moving from west to east across the delta's mangrove forest regions[35,36] (S9), significantly reducing the mangrove forest area by 0.15% (WGBMD) and 1.28% (EGBMD) (Fig. 2). The frequent occurrence of cyclones has undeniably exacerbated the vulnerability of mangroves.

Concurrently, relative sea-level rise (4.1 mm yr^{-1}) acts as a chronic force multiplier (Fig. S13), slightly exceeding the global average of approximately 3.1 mm yr^{-1} [37]. While sea-level rise is not the primary driver of mangrove retreat, evidenced by continued seaward expansion in certain areas, particularly at river mouths (Fig. 1C, Fig. S1), it acts as a key amplifier of wave-driven erosion. By deepening the water column at the mangrove toe, rising seas reduce the bottom friction that typically dissipates wave energy on tidal flats[38,39]. This coupling enables larger monsoon waves to propagate closer to the shoreline with undiminished power, intensifying scouring processes and accelerating retreat rates even under constant wave climates.

However, not all areas erode under high wave energy. In the EGBMD, Zones 5 and 8 showed a positive correlation between wave energy and accretion (Fig. S1B, Figs. S3–S9). This is likely due to the presence of offshore barrier islands. These islands shield the mangrove coast from direct wave impact, thereby promoting sediment deposition instead of erosion, even during high-energy periods.

Undeniably, tidal currents play a crucial role in the propagation and expansion of mangroves[40]. Upstream sediments are transported to the GBMD front, nearshore of the subaqueous delta, and the deep-sea Bengal Fan[41–45]. At the same time, relatively large tidal ranges (mean tidal range > 4 m)[46,47] intensify flood-tide currents, leading to the re-entry of some nearshore sediments into tidal channels. These sediments accumulate, narrowing the waterways and raising the elevation of the intertidal zone along the channel edges[48] (Fig. S14). This facilitates mangrove colonization, particularly in the WGBMD, similar to that observed in the Indus and Red River Deltas[23,49]. In general, this internal growth compensates for the losses along the seaward edge[50]. It can therefore be inferred that the blockage of tidal channels and the development of sandbanks are the primary drivers for the creation of environments favorable for mangrove expansion.

Fluvial sediment supplies

Riverine sediment supply is also crucial for balancing erosion. In the GBMD, approximately one-third of the riverine sediment is deposited directly within river channels or isolated within floodplains and delta plains due to tidal pumping[32]. However, the Ganges River and the Brahmaputra River showed a significant decreasing trend in suspended sediment discharge (SSD) over 32 years (Fig. S11A).

The mangrove response to this decline is not immediate. Our analysis reveals a strong positive correlation between sediment discharge and mangrove area ($r = 0.65$, $p < 0.001$) (Table S3), particularly in the EGBMD. The relation operates on an approximate 6-year cycle; sediment causes tidal flat accretion; this leads to bedforms like sandbars to form, and finally, mangrove propagules settle on these new landforms and gradually establish sizable communities. In our study, this is observed in the mangrove expansion following the peak sediment discharge in 2000 (Fig. 2A). Conversely, the current decline in mangrove area relates to the earlier fall in sediment supply. Such a time-lagged response of vegetation to environmental changes has also been confirmed in other studies[51–53].

Both natural cycles and human activities drive this sediment deficit. Naturally, major distributaries like the Bhagirathi-Hooghly have migrated eastward over time[54]. During non-monsoon periods, southward-flowing channels dry, leading to a sediment deficit in the WGBMD[45]. Human intervention exacerbates this trend. The Farakka Barrage (Fig. 1A), commissioned on the main channel of the Ganges River in 1975, diverts up to 1133 $m^3 s^{-1}$ of dry-season discharge from the Ganges main stem, leading to a ~43% reduction in downstream dry-season flow in Bangladesh and a consequent decline in sediment delivery to the WGBMD[55,56]. Local infrastructure, like polders, also disrupts natural deposition[57–60]. The reduction in upstream flow and associated sediment transport constrains sediment deposition at the delta front, making the mangrove more vulnerable to seaward erosion[61–63].

The seasonal sediment of sediment delivery likely provides a buffer to wave-induced erosion in the short-term, in addition to the longer channel and bank evolution process. During the monsoon (July–September), southwest waves are strongest, typically increasing erosion risk[64]. Yet, this period also coincides with the peak flux of suspended sediment (Fig. S11B). This high sediment concentration provides material for regeneration. It buffers the forest against wave damage[8]. In protected areas like the Sundarbans Reserve, this sediment helps mangroves recover from erosion and even expand seaward[65,66] (Fig. 1A). This sediment-driven process of mangrove expansion demonstrates the crucial role that sediment plays in buffering mangrove forests from wave-induced erosion and promoting their growth and proliferation.

Limitations

Our findings provide critical quantitative insights into the divergent morphodynamic responses of the GBMD mangroves to monsoon-driven wave energy and sediment supply, highlighting the complex resilience mechanisms of the world's largest deltaic mangrove system. However, accurately modeling these dynamics over a multi-decadal scale across such a complex mega-delta involves inherent challenges. To ensure a rigorous and balanced interpretation of the results, it is necessary to acknowledge specific limitations and potential biases associated with the datasets and methodological approaches utilized in this study:

1. Despite the extensive validation of ERA5 data in other regions, the spatial resolution of 0.5° × 0.5° may not fully capture fine-scale variations in wave height, particularly in coastal zones where the influence of local bathymetry and tides is significant. In addition, the interpolation procedure, particularly the use of Ordinary Kriging, may not adequately model the nonlinear wave transformation that occurs in shallow waters. This limitation, coupled with the lack of high-resolution local data, suggests that while ERA5 provides a useful proxy, it may introduce certain biases and uncertainties, particularly in nearshore areas. Consequently, derived wave energy values carry inherent uncertainties that should be considered when interpreting results.

2. Regarding the imagery, the Landsat series (MSS, TM, ETM+, OLI) was used to extract mangrove shorelines, with a spatial resolution of approximately 30 m. While this resolution is sufficient for large-scale analyses, it may not capture the finer details of complex shorelines. Specifically, dense tidal channel networks narrower than the pixel size (<30 m) are not individually resolved. Consequently, these micro-channels may be classified as a continuous mangrove forest, potentially leading to a slight overestimation of the total mangrove area. Future research could be improved by incorporating higher-resolution data, localized observations, and refined wave modeling techniques.

3. The primary drivers analyzed quantitatively in this study were incident wave energy and the long-term time-lagged effects of SSC. Specifically, the roles of tidal currents and mangrove biomass density were not directly quantified in the regression models. The importance of tidal currents in deltaic morphodynamics is widely acknowledged[67–69]. Their specific contribution to cross-shore shoreline change at the transect level was not modeled due to the lack of available high-resolution, long-term spatial current data required for direct integration into the analysis.

Conclusions

Located at the junction of India and Bangladesh, the Sundarbans mangrove forest in the GBMD is the world's largest mangrove ecosystem, renowned for its high ecological and socio-economic value. Here, based on a long-term series of remote sensing imagery, we quantitatively analyzed the dynamic changes in the mangrove forest area and its seaward edge, exploring the potential drivers of these changes. The key research findings are as follows:

1. The overall area of mangrove forests in the GBMD exhibited a fluctuating "M" shaped trend with an overall increase of 0.77%, corresponding to a change rate of 133.3 ± 6.7 ha yr^{-1}. Mangrove forest areas on

the EGBMD followed a similar trend. In contrast, the mangrove forest area on the WGBMD showed a stable decreasing trend. Changes in the mangrove forest area primarily occurred at the seaward edge rather than the landward edge.

2. The mangrove forests in the GBMD showed an overall seaward retreat rate of 5.98 ± 1.56 m yr^{-1}, even though mangrove shoreline erosion predominantly occurred in the WGBMD, while seaward expansion was mainly observed in the EGBMD. Meanwhile, erosion dominated the estuary areas of the WGBMD, while accretion was primarily distributed in the coastal islands and tidal flats of the EGBMD. Mangroves experienced a loss of 11,019.1 ha due to seaward retreat, while 2085.0 ha expanded seaward.

3. Mangrove seaward loss in the GBMD is primarily driven by persistent southwest monsoon-induced waves, with sea-level rise and cyclones acting as amplifiers. Upstream dam construction further reduces the downstream water and sediment supply, exacerbating the vulnerability of mangroves to erosion. In contrast, tidal currents have positively transported sediments into channels and backshore areas, narrowing tidal channels, as well as the presence of barrier islands, facilitating mangrove colonization. Mangrove expansion in the eastern region has outpaced the erosion in the west, primarily due to the consistent supply of sediment from rivers, which mitigates the effects of wave erosion. Moreover, natural reserves have been crucial in preventing internal mangrove losses.

These findings reveal the changing processes of GBMD mangrove forests and highlight the complex effects of both natural and human-driven factors. In particular, wave action contributes to shoreline retreat. Understanding these dynamics is crucial for developing effective conservation and restoration strategies tailored to the specific pressures faced by GBMD mangroves.

Materials and methods

Study area

The Ganges-Brahmaputra-Meghna Delta, located in South Asia, covers most of Bangladesh and the Indian state of West Bengal (Fig. 1A). It is the largest river delta in the world with an area of 105,000 km^2 [70]. The delta is formed by the confluence of three major rivers: the Ganges, the Brahmaputra, and the Meghna, which ultimately flow into the Bay of Bengal[70]. This delta extends eastward from the Hooghly River to the Meghna River. The Gorai-Madhumati River, a distributary of the Ganges, divides the GBMD into two distinct parts: the active eastern Ganges-Brahmaputra-Meghna Delta (EGBMD) and the less active western Ganges-Brahmaputra-Meghna Delta (WGBMD)[44,71,72] (Fig. 1A).

Mangrove extent extraction

This study utilizes all available Landsat remote sensing images from 1988 to 2022 for each scene, totaling 2729 images (Supplementary Note 1, Fig. S15), to extract and analyze the annual coverage of mangrove forests in the GBMD using the Google Earth Engine (GEE) platform (https://earthengine.google.com) (other relevant materials, see Supplementary Material). Specifically, the Landsat series of remote sensing images from 1988 to 2022 was synthesized by the Continuous Change Detection and Classification (CCDC) algorithm (Supplementary Note 2). CCDC, proposed by ref. 73, is a change detection algorithm based on time-series remote sensing data for detecting and classifying land surface changes (Table S4).

The Green, Red, Near-Infrared (NIR), Shortwave Infrared 1 (SWIR1), and Shortwave Infrared 2 (SWIR2) bands from Landsat were selected for analysis[74,75]. Additionally, due to the diverse land cover types in the GBMD, including mangrove forests, other vegetation, water bodies, buildings, and bare land, further indices were calculated to enhance classification features. These indices included: (1) the Normalized Difference Vegetation Index (NDVI) quantifies vegetation greenness by comparing near-infrared and red band[76]; (2) the Enhanced Vegetation Index (EVI) improves sensitivity in high biomass regions and minimizes atmospheric and soil background noise[77]; (3) the Land Surface Water Index (LSWI) is responsive to the liquid water content in vegetation and soil[78]; (4) the Modified Normalized Difference Water Index (mNDWI) enhances the identification of water bodies using green and shortwave infrared bands[79]; (5) the Mangrove Vegetation Index (MVI)[80], and (6) the Normalized Difference Mangrove Index (NDMI)[81] are tailored specifically for detecting and monitoring mangrove ecosystems.

Time series training samples from 1988 to 2022 were generated through (1) visual interpretation of 2022 synthesized remote sensing images and high-resolution historical Google Earth imagery, and (2) random sampling from the 2022 Global Mangrove Watch dataset, including mangrove and non-mangrove classes (water, tidal flat, pond, vegetation, bare land, and built-up). In total, more than 2300 sample points per year were collected (Table S5). Samples were randomly split into 80% for classifier training, while the remaining 20% for model accuracy validation. Subsequently, the coefficients of the time series model, the root mean square error of the model estimates, Landsat bands, spectral indices, and training sample points were used as inputs to the random forest classifier to obtain the spatiotemporal distribution of mangrove forests in the synthesized images from 1988 to 2022. The mangrove class had a producer's accuracy (PA) of 90.62–95.84% and a user's accuracy (UA) of 90.45–95.83% (Table S5). Only the mangrove class from the CCDC-derived classification was used, and misclassified or omitted mangrove areas were manually corrected based on actual image interpretation.

To clarify change processes, mangrove gains and losses across sequential study periods were quantified using the Erase function within the ArcGIS Overlay toolset, based on mangrove classification results. Specifically, the area of gain ($Area_{gain}$) was derived by erasing earlier-interval mangrove shapefiles from later-interval ones, while the area of loss ($Area_{loss}$) was calculated by erasing later-interval shapefiles from earlier-interval counterparts.

The total area of gain or loss ($Area_{total}$) was further categorized into seaward and non-seaward (internal) components:

$$Area_{total} = Area_{seaward} + Area_{non-seaward} \quad (1)$$

where $Area_{seaward}$ represents the area of gain or loss occurring along the seaward margin, and $Area_{non-seaward}$ represents the gain or loss in non-seaward (e.g., tidal channel or interior) regions. Note that in this study, "total gain" refers to the gross expansion of mangrove area, while "total loss" refers to the gross retreat, distinct from the arithmetic net change.

Mangrove shoreline extraction

In the context of this study, the term 'shoreline' refers exclusively to the seaward limit of the mangrove vegetation. This proxy was selected to capture the morphodynamic response of the forest fringe to hydrodynamic forcing, distinct from the physical water-land boundary.

Based on the visually corrected mangrove classification raster and concerning the original false-color composite images, the digital mangrove shoreline for each year from 1988 to 2022 was extracted in ArcGIS through a workflow: (1) the classified raster was converted to polygons using the Raster to Polygon tool; (2) these polygons were converted to line features using the Polygon to Line tool; and (3) the seaward edge of each mangrove polygon was manually identified and retained. To minimize digitization errors, all delineation steps were performed by the same individual.

The quantitative analysis of mangrove shorelines utilized the Digital Shoreline Analysis System (DSAS) developed by the United States Geological Survey (USGS). DSAS employs regression analysis to calculate mangrove shoreline change rates, thereby quantitatively revealing the historical shoreline changes over extensive areas and long periods[20,40,82]. Using DSAS, we established a baseline parallel to the shoreline at the landward edge, generating 15,433 transects perpendicular to the baseline at 30-meter intervals, extending from landward to seaward and from west to east. Given the irregular shape of the shoreline, overlapping and intersecting transects were adjusted to retain only accurate ones.

Mangrove shoreline change metrics were calculated following Himmelstoss et al.[83]. Net Shoreline Movement (NSM) represents the long-term net shoreline change from 1988 to 2022 (in meters). Shoreline Change

Envelope (SCE) captures the maximum positional variability over the study period. End Point Rate (EPR) measures the change rate between the oldest (1988) and most recent (2022) shorelines. End Point Rate (EPR) and weighted linear regression rate (WLR) represent the shoreline change rates, with EPR considering the change rate between the oldest (1988) and most recent (2022) shorelines, while the Weighted Linear Regression rate (WLR) quantifies long-term shoreline changes using annual shoreline data and accounts for uncertainties (Supplementary Note 3, Table S6) in annual positions. Change rates are expressed as negative and positive values in m per year (m yr^{-1}), where negative values indicate retreat and positive values indicate advance.

The formula for calculating the seaward gain or loss of the mangrove area is as follows:

$$Area_{seaward} = \begin{cases} \sum NSM_{EPR>0} D_T, Area_{s(gain)} \\ \sum NSM_{EPR<0} D_T, \ Area_{s(loss)} \end{cases} \quad (2)$$

where $NSM_{EPR>0}$ is the NSM when the shorelines of 1988 and 2022 move seaward (EPR > 0), $NSM_{EPR<0}$ is the NSM when the shorelines of 1988 and 2022 move landward (EPR < 0), and D_T is the transect spacing (30 m in this study).

Hydrodynamics analysis

Wave data were obtained from the ERA5 reanalysis produced by the European Centre for Medium-Range Weather Forecasts (ECMWF). ERA5 combines historical model forecasts with in-situ observations to reduce biases and fill data gaps. Due to the absence of long-term in-situ nearshore wave measurements across the study area, ERA5 was used as a proxy for nearshore wave conditions. Significant wave height (SWH) and mean wave direction (MWD) from 1988–2022 were extracted for the Ganges–Brahmaputra–Meghna Delta (86.71°–92.63°E, 19.59°–23.95°N). Previous studies validated the ERA5-derived significant wave height and wave direction against in situ observations in the Bay of Bengal. These comparisons show high agreement. The correlation coefficients typically exceed 0.9[84,85]. These results support the applicability of ERA5 data for hydrodynamics analysis in the GBMD.

To characterize seasonal wave forcing, hourly ERA5 SWH and MWD at each grid point (Fig. 1A) were first aggregated in MATLAB to obtain annual monsoon-season (June–September) and non-monsoon (October–May) mean wave heights, as well as the 95th-percentile wave height representing extreme events. The mean SWH was calculated as:

$$\bar{H} = \frac{1}{n}\sum_{i=1}^{n} H_i \quad (3)$$

where H_i is the hourly wave height, and n is the total number of hours in the period. The 95th percentile wave height (H_{95}) was determined such that 95% of hourly wave heights fall below it.

For each year, these aggregated values were interpolated using Ordinary Kriging in the ArcGIS Geostatistical Analyst toolbox to generate continuous geostatistical layers for the monsoon and non-monsoon seasons (interpolation RMSE is listed in Table S7). Shoreline transects were represented by their midpoints, from which wave-height values were extracted using the GA Layer to Points tool. For each transect, the multi-year mean wave height was then converted into wave energy density (E) based on linear wave theory[86]. The calculation uses the following simplified formulation:

$$E = \frac{1}{8}\rho g \bar{H}^2 \quad (4)$$

where ρ represents the seawater density (1025 kg m^{-3}) and g represents the gravitational acceleration (9.81 m s^{-2}). We applied these wave-energy metrics in a regression analysis. This analysis assessed the influence of wave energy on mangrove shoreline change.

To assess the potential influence of sediment supply on mangrove dynamics, we conducted a lagged correlation analysis using annual mangrove area change ($\Delta Area_t$) and suspended sediment discharge (SSD) in the Ganges, Brahmaputra, and Meghna Rivers. Annual mangrove area change was calculated as:

$$\Delta Area_t = Area_t - Area_{t-1} \quad (5)$$

where $Area_t$ and $Area_{t-1}$ are mangrove areas in the current and previous year, respectively. The lagged Pearson correlation coefficient between $\Delta Area_t$ and SSD was calculated as:

$$r(lag) = \frac{Cov\left(\Delta Area_{t-lag}, SSD_t\right)}{\sigma \Delta Area_{t-lag} \cdot \sigma_{SSD_t}} \quad (6)$$

where $\Delta Area_{t-lag}$ is the mangrove area change series shifted backward by lag years, SSD_t is the suspended sediment discharge in year t, Cov is the covariance, and σ denotes standard deviation. Correlations were computed for lags from 0 to 10 years to identify the interval at which SSD most strongly influenced mangrove area change. Analyses were conducted for the entire delta and for subregions to assess spatial variability in the relationship.

Data availability

The Landsat satellite imagery used in this study is available from the USGS Earth Explorer (https://earthexplorer.usgs.gov/) and the Google Earth Engine data catalog. The Global Mangrove Watch (GMW) dataset is available at https://www.globalmangrovewatch.org/. Wave energy data (ERA5) can be accessed via the Copernicus Climate Change Service (https://cds.climate.copernicus.eu/). Sea-level rise data are available from the NOAA Laboratory for Satellite Altimetry (https://www.star.nesdis.noaa.gov/socd/lsa/SeaLevelRise/). Typhoon track data are available from IBTrACS (https://www.ncei.noaa.gov/products/international-best-track-archive). The bathymetric data were obtained from the UK Hydrographic Office (https://www.gov.uk/government/organisations/uk-hydrographic-office) (restrictions apply to redistribution). Source data underlying the graphs and charts in the main text are provided as Supplementary Data 1.

Code availability

The mangrove classification and change detection were performed using Google Earth Engine (GEE) API. The shoreline change rates were calculated using the Digital Shoreline Analysis System (DSAS v5.0), which is publicly available at https://www.usgs.gov/centers/whcmsc/science/digital-shoreline-analysis-system-dsas. The calculation of wave energy flux followed standard formulations as described in the "Methods".

Received: 8 August 2025; Accepted: 4 March 2026;
Published online: 24 March 2026

References

1. Hogarth, P. J. In *Encyclopedia of Biodiversity* 2nd edn (ed. Levin, S. A) 10 (Academic Press, 2013).
2. Jia, M. et al. Mapping global distribution of mangrove forests at 10-m resolution. *Sci. Bull.* **68**, 1306 (2023).
3. Duarte, C. M. & Cebrián, J. The fate of marine autotrophic production. *Limnol. Oceanogr.* **41**, 1758 (1996).
4. Wang, F., Cheng, P., Chen, N. & Kuo, Y. Tidal driven nutrient exchange between mangroves and estuary reveals a dynamic source-sink pattern. *Chemosphere* **270**, 128665 (2021).
5. Akram, H. et al. Mangrove health: a review of functions, threats, and challenges associated with mangrove management practices. *Forests* **14**, 1698 (2023).

6. Bunting, P. et al. Global mangrove extent change 1996–2020: global mangrove watch version 3.0. *Remote Sens.* **14**, 3657 (2022).
7. Zhao, B., Lei, H., Yang, D., Yang, S. & Santisirisomboon, J. Runoff and sediment response to deforestation in a large Southeast Asian monsoon watershed. *J. Hydrol.* **606**, 127432 (2022).
8. Dai, Z., Long, C., Mei, X., Fagherazzi, S. & Xiong, Y., Overestimation of mangroves deterioration from sea level rise in tropical deltas. *Geophys. Res. Lett.* **51**, e2024GL109675 (2024).
9. Swales, A., Bentley, S. J. Sr & Lovelock, C. E. Mangrove-forest evolution in a sediment-rich estuarine system: opportunists or agents of geomorphic change? *Earth Surf. Process. Landf.* **40**, 1672 (2015).
10. Gijsman, R. et al. Mangrove forest drag and bed stabilisation effects on intertidal flat morphology. *Earth Surf. Process. Landf.* **49**, 1117 (2024).
11. Balke, T. et al. Windows of opportunity: tresholds to mangrove seedling establishement on tidal flats. *Mar. Ecol. Prog. Ser.* **440**, 1 (2011).
12. Nath, A. et al. Erosion hotspots and the drivers of erosion along the part of West Bengal coast, India. In *Problematic Soils and Geoenvironmental Concerns* (eds Gali, M. L. & Rao, P. R.) Vol. 88, 193–207 (Springer, 2021).
13. Le, T. X., Schwarzer, K., Nguyen, T. C., Bui, L. T. & Unverricht, D. Late Holocene morphodynamic feedback in Can Gio mangrove tide-dominated river mouth systems, Vietnam. *Coasts* **2**, 221–243 (2022).
14. Toorman, E. A. et al. in *Threats to Mangrove Forests: Hazards, Vulnerability, and Management* (eds Makowski, C. & Finkl, C. W.) 429 (Springer International Publishing, 2018).
15. Spencer, T., Möller, I. & Reef, R. in *Reference Module in Earth Systems and Environmental Sciences* (Elsevier, 2016).
16. Wang, J. et al. Large-scale sedimentary shift induced by a mega-dam in deltaic flats. *Sedimentology* **71**, 1084 (2024).
17. Richards, D. R., Thompson, B. S. & Wijedasa, L. Quantifying net loss of global mangrove carbon stocks from 20 years of land cover change. *Nat. Commun.* **11**, 4260 (2020).
18. van Bijsterveldt, C. E. J. et al. Subsidence reveals potential impacts of future sea level rise on inhabited mangrove coasts. *Nat. Sustain.* **6**, 1565 (2023).
19. Lagomasino, D. et al. Storm surge and ponding explain mangrove dieback in southwest Florida following Hurricane Irma. *Nat. Commun.* **12**, 4003 (2021).
20. Xiong, Y. et al. Machine learning-based examination of recent mangrove forest changes in the western Irrawaddy River Delta, Southeast Asia. *Catena* **234**, 107601 (2024).
21. Arifanti, V. B. et al. Contributions of mangrove conservation and restoration to climate change mitigation in Indonesia. *Glob. Chang. Biol.* **28**, 4523 (2022).
22. Hagger, V. et al. Drivers of global mangrove loss and gain in social-ecological systems. *Nat. Commun.* **13**, 6373 (2022).
23. Zhou, Y., Dai, Z., Liang, X. & Cheng, J. Machine learning-based monitoring of mangrove ecosystem dynamics in the Indus Delta. *For. Ecol. Manag.* **571**, 122231 (2024).
24. Phan, M. H. & Stive, M. J. F. Managing mangroves and coastal land cover in the Mekong Delta. *Ocean Coast. Manag.* **219**, 106013 (2022).
25. Sarwar, M. G. M. & Woodroffe, C. D. Rates of shoreline change along the coast of Bangladesh. *J. Coast. Conserv.* **17**, 515 (2013).
26. Sarwar, M. G. M. & Islam, A. Multi hazard vulnerabilities of the coastal land of Bangladesh. In *Climate Change Adaptation Actions in Bangladesh* (eds Shaw, R., Mallick, F. & Islam, A.) 121–141 (Springer, 2013).
27. Sarwar, M. G. M. Sea-level rise along the coast of Bangladesh. In *Disaster Risk Reduction Approaches in Bangladesh* (eds Shaw, R., Mallick, F. & Islam, A.) 217–232 (Springer, 2013).
28. Mahmood, H. et al. Paradigm shift in the management of the Sundarbans mangrove forest of Bangladesh: Issues and challenges. *Trees For. People* **5**, 100094 (2021).
29. Rogers, K. G. & Goodbred, S. L. In *Landscapes and Landforms of India* (ed. Kale, V. S.) 181 (Springer Netherlands, 2014).
30. Vinayachandran, P. N., Masumoto, Y., Mikawa, T. & Yamagata, T. Intrusion of the Southwest Monsoon Current into the Bay of Bengal. *J. Geophys. Res. Oceans* **104**, 11077 (1999).
31. Elahi, M. W. E., Wang, X. H. & Ritchie, E. A. Cyclone-induced storm surge flooding in the Ganges-Brahmaputra-Meghna delta under different mean-sea level rise scenarios. *Ocean Dynam.* **75**, 27 (2025).
32. Raff, J. L. et al. Sediment delivery to sustain the Ganges-Brahmaputra delta under climate change and anthropogenic impacts. *Nat. Commun.* **14**, 2429 (2023).
33. Ali, M. I., Saifullah, M., Imran, A., Syed, I. M. & Mallik, M. A. K. Studying the Intensity and Storm Surge Phenomena of Tropical Cyclone Roanu (2016) over the Bay of Bengal Using NWP Model. *J. Sci. Res.* **12**, 55 (2020).
34. Hossain, M. A. et al. Storm surge simulation of cyclone "Roanu" over coastal regions of Bangladesh using MRI storm surge model. *DEW-DROP* **1**, 1–12 (2017).
35. Das, G. K. Cyclonic hazards in the recent past in peninsular India. *Reason-A Tech. J.* **19**, 1–15 (2021).
36. Krishnaja, P. B., Akhila, R. S., Kuttippurath, J. & Sunanda, N. Tropical cyclone-driven rainfall in the northeast Indian Ocean and adjoining land regions during the period 2000–2020. *J. Hydrol.* **629**, 130610 (2024).
37. Fox-Kemper, B. et al. Ocean, cryosphere and sea level change. In *Climate Change 2021: The Physical Science Basis. Contribution of Working Group I to the Sixth Assessment Report of the Intergovernmental Panel on Climate Change* (eds Masson-Delmotte, V. et al.) 1211–1362 (Cambridge University Press, 2021).
38. Zhou, X., Dai, Z., Pang, W., Wang, J. & Long, C. Wave attenuation over mangroves in the Nanliu Delta. *China Front. Mar. Sci.* **9**, 874818 (2022).
39. Mariotti, G. & Fagherazzi, S. A numerical model for the coupled long-term evolution of salt marshes and tidal flats. *J. Geophys. Res. Earth Surf.* **115**, F01004 (2010).
40. Long, C. et al. Dynamic changes in mangroves of the largest delta in northern Beibu Gulf, China: reasons and causes. *For. Ecol. Manag.* **504**, 119855 (2022).
41. Fischer, S., Pietroń, J., Bring, A., Thorslund, J. & Jarsjö, J. Present to future sediment transport of the Brahmaputra River: reducing uncertainty in predictions and management. *Reg. Environ. Chang.* **17**, 515 (2017).
42. Krien, Y. et al. Present-day subsidence in the Ganges-Brahmaputra-Meghna Delta: eastern amplification of the holocene sediment loading contribution. *Geophys. Res. Lett.* **46**, 10764 (2019).
43. Mitra, A. in *Estuarine Pollution in the Lower Gangetic Delta: Threats and Management* (ed. Mitra, A.) 1 (Springer International Publishing, 2019).
44. Paszkowski, A., Goodbred, S., Borgomeo, E., Khan, M. S. A. & Hall, J. W. Geomorphic change in the Ganges–Brahmaputra–Meghna delta. *Nat. Rev. Earth Environ.* **2**, 763 (2021).
45. Rahman, M. et al. Recent sediment flux to the Ganges-Brahmaputra-Meghna delta system. *Sci. Total Environ.* **643**, 1054 (2018).
46. Bandyopadhyay, S., Kar, N. S., Dasgupta, S., Mukherjee, D. & Das, A. Island area changes in the Sundarban region of the abandoned western Ganga–Brahmaputra–Meghna Delta, India and Bangladesh. *Geomorphology* **422**, 108482 (2023).
47. Bricheno, L. M., Wolf, J. & Islam, S. Tidal intrusion within a mega delta: an unstructured grid modelling approach. *Estuar. Coast. Shelf Sci.* **182**, 12 (2016).
48. Hughes, Z. J. in *Principles of Tidal Sedimentology* (eds Davis Jr. R. A. & Dalrymple, R. W.) 269 (Springer Netherlands, 2012).
49. Long, C., Dai, Z., Zhou, X., Mei, X. & Mai Van, C. Mapping mangrove forests in the Red River Delta, Vietnam. *For. Ecol. Manag.* **483**, 118910 (2021).

50. FitzGerald, D. M. Shoreline erosional–depositional processes associated with tidal inlets. In *Hydrodynamics and Sediment Dynamics of Tidal Inlets* (eds Aubrey, D. G. & Weishar, L.) Vol. 29, 186–225 (Springer, 1988).
51. Anthony, E. J. et al. Sustainable management, conservation, and restoration of the Amazon River Delta and Amazon-influenced Guianas coast: a review. *Water*. **13**, 1371 (2021).
52. Gao, J., Kennedy, D. M. & McSweeney, S. Decadal changes in vegetation cover within coastal dunes at the regional scale in Victoria, SE Australia. *J. Environ. Manag.* **351**, 119622 (2024).
53. Asbridge, E., Lucas, R., Ticehurst, C. & Bunting, P. Mangrove response to environmental change in Australia's Gulf of Carpentaria. *Ecol. Evol.* **6**, 3523 (2016).
54. Kuehl, S. A., Levy, B. M., Moore, W. S. & Allison, M. A. Subaqueous delta of the Ganges-Brahmaputra river system. *Mar. Geol.* **144**, 81 (1997).
55. Mirza, M. M. Q. Diversion of the Ganges Water at Farakka and its effects on salinity in Bangladesh. *Environ. Manag.* **22**, 711 (1998).
56. Rahman, M. M. & Rahaman, M. M. Impacts of Farakka barrage on hydrological flow of Ganges river and environment in Bangladesh. *Sustain. Water Resour. Manag.* **4**, 767 (2018).
57. Brammer, H. Bangladesh's dynamic coastal regions and sea-level rise. *Clim. Risk Manag.* **1**, 51 (2014).
58. Nath, S., van Laerhoven, F. & Driessen, P. P. J. Have Bangladesh's polders decreased livelihood vulnerability? A comparative case study. *Sustainability* **11**, 7141 (2019).
59. Islam, S. *Unraveling KJDRP: ADB Financed Project of Mass Destruction in Southwest Coastal Region of Bangladesh* (Uttaran, 2006).
60. Shahjahan Mondal, M. et al. in *Confronting Climate Change in Bangladesh: Policy Strategies for Adaptation and Resilience* (ed Huq, S. et al.) 7 (Springer International Publishing, 2019).
61. Rogers, K. G. & Overeem, I. Doomed to drown? Sediment dynamics in the human-controlled floodplains of the active Bengal Delta. *Elem. Sci. Anth.* **5**, 66 (2017).
62. Islam, M. F., Schot, P. P., Dekker, S. C., Griffioen, J. & Middelkoop, H. Physical controls and a priori estimation of raising land surface elevation across the southwestern Bangladesh delta using tidal river management. *Hydrol. Earth Syst. Sci.* **26**, 903 (2022).
63. Rahman, A. F., Dragoni, D. & El-Masri, B. Response of the Sundarbans coastline to sea level rise and decreased sediment flow: a remote sensing assessment. *Remote Sens. Environ.* **115**, 3121 (2011).
64. Wang, Z., Yu, M., Dong, S., Wu, K. & Gong, Y. Wind and wave climate characteristics and extreme parameters in the Bay of Bengal. *Reg. Stud. Mar. Sci.* **39**, 101403 (2020).
65. Aziz, A. & Paul, A. R. Bangladesh Sundarbans: present status of the environment and biota. *Diversity* **7**, 242–269 (2015).
66. Chauhan, M. & Gopal, B. in *Our National River Ganga: Lifeline of Millions*, (ed Sanghi, R.) 143 (Springer International Publishing, Cham, 2014).
67. Finotello, A., Lentsch, N. & Paola, C. Experimental delta evolution in tidal environments: morphologic response to relative sea-level rise and net deposition. *Earth Surf. Process. Landf.* **44**, 2000 (2019).
68. Zhang, X., Fagherazzi, S., Leonardi, N. & Li, J. A positive feedback between sediment deposition and tidal prism may affect the morphodynamic evolution of tidal deltas. *J. Geophys. Res. Earth Surf.* **123**, 2767 (2018).
69. Hoitink, A. J. F., Wang, Z. B., Vermeulen, B., Huismans, Y. & Kästner, K. Tidal controls on river delta morphology. *Nat. Geosci.* **10**, 637 (2017).
70. Fergusson, J. On recent changes in the Delta of the Ganges. *Q. J. Geol. Soc. Lond.* **19**, 321 (1863).
71. Islam, S. N. & Gnauck, A. Mangrove wetland ecosystems in Ganges-Brahmaputra delta in Bangladesh. *Front. Earth Sci. China* **2**, 439 (2008).
72. Islam, S. N. Deltaic floodplains development and wetland ecosystems management in the Ganges–Brahmaputra–Meghna Rivers Delta in Bangladesh. *Sustain. Water Resour. Manag.* **2**, 237 (2016).
73. Zhu, Z. & Woodcock, C. E. Continuous change detection and classification of land cover using all available Landsat data. *Remote Sens. Environ.* **144**, 152 (2014).
74. Li, X. et al. The importance of adding short-wave infrared bands for forest disturbance monitoring in the subtropical region. *Sustainability* **14**, 10312 (2022).
75. Chastain, R., Housman, I., Goldstein, J., Finco, M. & Tenneson, K. Empirical cross sensor comparison of Sentinel-2A and 2B MSI, Landsat-8 OLI, and Landsat-7 ETM+ top of atmosphere spectral characteristics over the conterminous United States. *Remote Sens. Environ.* **221**, 274 (2019).
76. Tucker, C. J. Red and photographic infrared linear combinations for monitoring vegetation. *Remote Sens. Environ.* **8**, 127 (1979).
77. Huete, A. et al. Overview of the radiometric and biophysical performance of the MODIS vegetation indices. *Remote Sens. Environ.* **83**, 195 (2002).
78. Chandrasekar, K., Sesha Sai, M. V. R., Roy, P. S. & Dwevedi, R. S. Land Surface Water Index (LSWI) response to rainfall and NDVI using the MODIS Vegetation Index product. *Int. J. Remote Sens.* **31**, 3987 (2010).
79. Xu, H. Modification of normalised difference water index (NDWI) to enhance open water features in remotely sensed imagery. *Int J. Remote Sens.* **27**, 3025 (2006).
80. Baloloy, A. B., Blanco, A. C., Sta, Ana, R. R. C. & Nadaoka, K. Development and application of a new mangrove vegetation index (MVI) for rapid and accurate mangrove mapping. *ISPRS J. Photogramm. Remote Sens.* **166**, 95 (2020).
81. Shi, T. et al. New spectral metrics for mangrove forest identification. *Remote Sens. Lett.* **7**, 885 (2016).
82. Nassar, K. et al. Shoreline change detection using DSAS technique: case of North Sinai coast, Egypt. *Mar. Georesour. Geotechnol.* **37**, 81 (2019).
83. Himmelstoss, E. A., Henderson, R. E., Kratzmann, M. G. & Farris, A. S. Digital Shoreline Analysis System (DSAS) version 5.1 user guide. (U.S. Geological Survey Open-File Report 2021–1091, 2021).
84. Sreelakshmi, S. & Bhaskaran, P. K. Wind-generated wave climate variability in the Indian Ocean using ERA-5 dataset. *Ocean Eng.* **209**, 107486 (2020).
85. Kumari, A., Kumar, S. P. & Chakraborty, A. Seasonal and interannual variability in the barrier layer of the Bay of Bengal. *J. Geophys. Res. Oceans* **123**, 1001 (2018).
86. Dean, R. G. & Dalrymple, R. A. *Water Wave Mechanics For Engineers And Scientists* (World Scientific Publishing Company, 1991).

Acknowledgements

We would like to thank Professor Colin Woodroffe from the University of Wollongong for his valuable suggestions and insightful comments, which greatly contributed to the improvement of this manuscript. We also gratefully acknowledge Associate Professor Rongyong Huang from the School of Marine Sciences, Guangxi University, for his constructive and meaningful suggestions on the wave-related issues. Funding: This research was supported by the National Natural Science Key Foundation of China (NSFC) (41930537), the Shanghai International Science and Technology Cooperation Fund Project (23230713800; 24230740100), and 2024 International Cooperation Seed Funding Project for China's Ocean Decade Actions (GHZZ370284000202402000025).

Author contributions

Conceptualization: Z.D. Methodology: Y.X., Z.D., and C.L. Formal analysis: Y.X. and Z.D. Data curation: Y.X Writing—original draft: Y.X., Z.D. Writing—review and editing: Z.D., C.L., X.M., J.C., and D.K. Visualization: Y.X., C.V., and B.N. Supervision: Z.D. Funding acquisition: Z.D.

Competing interests

The authors declare no competing interests.

Additional information

Supplementary information The online version contains supplementary material available at https://doi.org/10.1038/s43247-026-03397-z.

Correspondence and requests for materials should be addressed to Zhijun Dai.

Peer review information *Communications Earth and Environment* thanks the anonymous reviewers for their contribution to the peer review of this work. Primary Handling Editors: Adam Switzer and Somaparna Ghosh A peer review file is available.